INORGANIC CHEMISTRY FRONTIERS

RESEARCH ARTICLE

View Article Online
View Journal | View Issue

Cite this: *Inorg. Chem. Front.*, 2026, **13**, 1568

Universal upconversion amplification *via* 4d–4f hybridization in Ln^{3+}/MoO_4^{2-} co-doped fluorapatite: mechanism and applications

Boyang Wang,[a] Yuankun Ren,[a] Xiaohan Wei,[a] Wei Yang,[a] Haoming Su,[b] Yu Liu,[a] Jiaqi Liang[a] and Xiyu Li *[a]

Received 17th September 2025,
Accepted 3rd December 2025

DOI: 10.1039/d5qi01918d

rsc.li/frontiers-inorganic

Lanthanide-doped fluorapatite (FAp:Ln^{3+}) upconversion luminescence (UCL) probes exhibit good biocompatibility but suffer from low quantum yields under near-infrared (NIR) excitation. Here, we propose a universal MoO_4^{2-} doping strategy that achieves 74-fold green UCL enhancement in FAp:Yb/Er/Mo (FYEM) under 980 nm excitation (quantum yield: 0.004% at 50 W cm^{-2}). Remarkably, stable Ln^{3+}/MoO_4^{2-} dimers induce 4d–4f orbital hybridization, as validated by density functional theory (DFT) and X-ray photoelectron spectroscopy (XPS). This mechanism extends to self-sensitized systems: FAp:Er/Mo (FEM) achieves 156-fold UCL enhancement under 980 nm excitation, while FAp:Nd/Mo (FNM) integrates 84-fold UCL amplification with photothermal synergy (ΔT = 53.5 °C). Critically, the optimized FYEM material enables dual-mode imaging, with 808/980 nm excitation UCL and NIR-II downconversion luminescence for deep-tissue imaging, besides outstanding thermal sensitivity (S_A = 1.04% K^{-1}@323 K). This work establishes a biocompatible, multi-wavelength platform for deep-tissue diagnostics, photothermal therapy, and multimodal sensing and imaging.

1. Introduction

Upconversion luminescence (UCL), which converts near-infrared (NIR) photons to higher-energy visible emissions, offers advantages for biomedical imaging, including deep-tissue penetration and minimized photodamage.[1–3] Among biocompatible matrices, fluorapatite (FAp) stands out due to its intrinsic bone affinity, biodegradability, and critically lower lattice phonon energy compared to hydroxyapatite (HAp).[4–6] This arises from F^- substitution for the OH^- groups, reducing vibrational quenching (~1000 cm^{-1} for F^- *vs.* 2700–3700 cm^{-1} for OH^-). Nevertheless, FAp:Ln^{3+} suffers from low fluorescence intensity and critically low upconversion quantum yields under NIR excitation, limiting clinical translation. Conventional enhancement strategies involving transition metal (TM) cation doping (*e.g.*, Fe^{3+}, Mn^{2+}) often face critical limitations,[7,8] because TM ions could induce parasitic visible-light absorption, causing spectral overlap with emission bands and fluorescence quenching.[9] Recent studies suggest d^0-centered oxyanions (*e.g.*, MoO_4^{2-}) may circumvent these limitations. Van *et al.* demonstrated UCL enhancement in MoO_4^{2-}-doped HAp/β-TCP composites *via* Ln^{3+}/MoO_4^{2-} dimers.[10] But the high phonon energy of these matrices restricts efficiency, and the atomic-scale enhancement mechanism remains unearthed. Critically, FAp's lower phonon energy provides untapped potential for greater enhancement, and MoO_4^{2-} doping in Ln-doped FAp has not been systematically explored.

Herein, we propose a novel MoO_4^{2-} doping strategy to harness its phononic advantage. By substituting PO_4^{3-} with MoO_4^{2-}, FAp:Yb/Er/Mo (FYEM) achieves a 74-fold green UCL enhancement under 980 nm excitation (UCQY: 0.004%), and a 287-fold amplification under 808 nm excitation. These enhancements stem from 4d–4f orbital hybridization mediated by stable Ln^{3+}/MoO_4^{2-} dimers, as validated by X-ray photoelectron spectroscopy (XPS) and density functional theory (DFT). XPS analysis reveals MoO_4^{2-}-driven electron redistribution, while DFT confirms that MoO_4^{2-} preferentially occupies the PO_4^{3-} adjacent to Yb^{3+}, broadening the 4f density of states near the Fermi level. This strategy could extend to self-sensitized systems. FAp:Er/Mo (FEM) exhibits a 156-fold UCL enhancement under 980 nm excitation, while FAp:Nd/Mo (FNM) integrates an 84-fold UCL amplification with synergetic photothermal conversion capability (ΔT = 53.5 °C). Critically, FAp:Nd/Yb/Er/Mo (FNYEM) achieves simultaneous excitation at both 808 nm and 980 nm, delivering strong UCL while preserving spectral purity, thereby eliminating laser-induced over-

[a]*State key Laboratory of Oral Diseases & National Center for Stomatology & National Clinical Research Center for Oral Diseases, West China Hospital of Stomatology, Sichuan University, Chengdu, Sichuan, 610041, China*
[b]*Department of Chemistry, Tufts University, Medford, MA, 02155, USA*

heating risks. FYEM also demonstrates dual-mode imaging capabilities, combining visible UCL (510–570 nm) and NIR-II downconversion luminescence (DCL) (1450–1650 nm) for deep-tissue imaging. Additionally, green UCL of FYEM exhibits outstanding thermal sensitivity under physiological temperature (283–323 K), with maximum absolute sensitivity (S_A) = 1.04% K^{-1}; maximum relative sensitivity (S_R) = 1.28% K^{-1}, outperforming existing similar sensors including $NaYF_4$ and Ca_2MgWO_6.

This work addresses three critical challenges in UCL design: (1) reconciling luminescent efficiency and versatility through MoO_4^{2-} co-doping; (2) elucidating the atomic-scale mechanism of 4d–4f hybridization *via* XPS/DFT validation; (3) establishing a universal enhancement paradigm for diverse Ln^{3+} systems (Er^{3+}, Ho^{3+}, Tm^{3+}). By integrating multi-wavelength excitation (808/980 nm), photothermal synergy, and multimodal sensing, our strategy enables transformative advances in deep-tissue theranostics.

2. Results

2.1. Morphology and structural characterization

All samples were synthesized *via* a facile one-pot hydrothermal method followed by thermal activation at 900 °C (Fig. 1a). X-ray diffraction (XRD) patterns (Fig. 1b and S1) confirm the hexagonal fluorapatite structure (*P*63/*m* space group) for all samples, with characteristic peaks at 25.9° (002), 31.9° (211), 32.3° (112), 33.1° (300), 40° (310), 46.8° (222), and 49.6° (213). Co-doping with Ln^{3+} (Yb^{3+}/Er^{3+}, Yb^{3+}/Ho^{3+}, Yb^{3+}/Tm^{3+}) and MoO_4^{2-} shifts diffraction peaks toward higher 2θ values (Fig. 1b and S1), indicating lattice contraction due to the smaller ionic radii of dopants *versus* Ca^{2+} and PO_4^{3-}. Aliovalent substitution (MoO_4^{2-} for PO_4^{3-}) also induces impurity phases in samples (minor $CaMoO_4$ and $CaCO_3$, denoted by symbols in Fig. 1b and S2) in MoO_4^{2-}-doped samples. To quantify the relative phase content and confirm fluorapatite remains the main phase, we conducted Rietveld refinement on

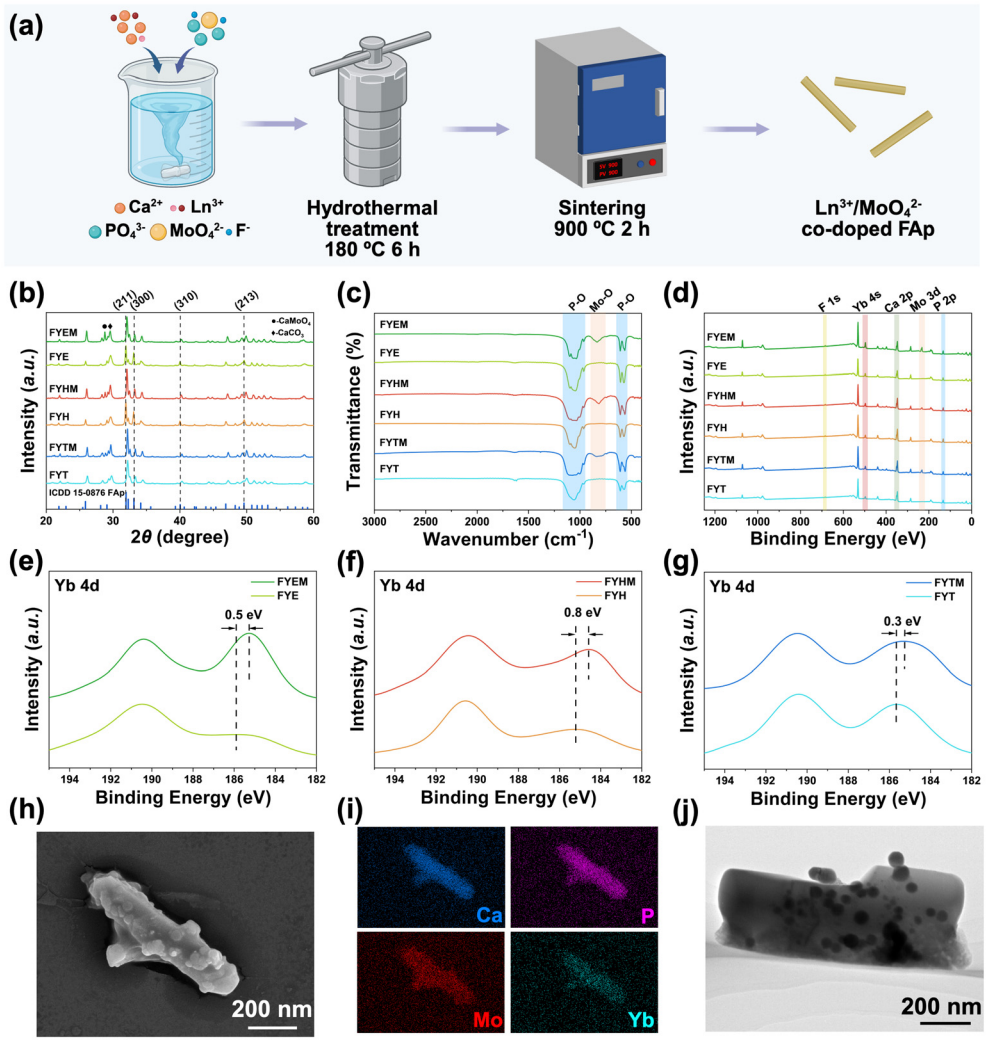

Fig. 1 (a) Flow chart of the synthesis procedure. (b) XRD patterns of FYX and FYXM samples (F-FAp, Y-Yb, X-(Er, Ho, or Tm), M-Mo). (c) FTIR spectra of FYX and FYXM samples. (d) XPS survey spectra of FYX and FYXM samples. (e–g) Yb 4d XPS high-resolution spectra of FYX and FYXM samples. (h) SEM image of FYEM. (i) Element mapping of FYEM. (j) TEM image of FYEM.

the XRD data of FYEM as given in Fig. S2 and Table S3. The refinement indicates that the dominant phase is the intended fluorapatite with a weight percentage of ~93.9%, suggesting co-doped fluorapatite remains the dominant phase. Fourier transform infrared (FTIR) spectra (Fig. 1c and S3, Table S4) reveal characteristic vibrational modes of PO_4^{3-} group (606–609 and 950–1100 cm^{-1}). Mo-doped samples exhibit additional peaks at 830–850 cm^{-1} attributed to $\nu_3(MoO_4)$, corroborating successful doping of MoO_4^{2-}.[11] The stretching and bending bands remarkably broaden in the range of 950–1100 cm^{-1} after doping MoO_4^{2-}, indicating local lattice distortion and symmetry breaking, and possible formation of charge-compensation defects. A slight vibration mode of CO_3^{2-} from $CaCO_3$ secondary phase can be observed in the range of 1400–1500 cm^{-1}, possibly caused by recombination of CO_2 in air upon cooling after sintering. Thermogravimetric (TG-DSC) analysis was conducted to confirm thermal stability of samples under 900 °C (Fig. S4). XPS spectra (Fig. 1d and S5) confirm successful dopant incorporation. High-resolution XPS spectra reveal electron redistribution. Notably, compared with Mo-free FYX groups, Yb 4d binding energies shift negatively by 0.3–1.1 eV in Mo-doped FYXM groups (Fig. 1e–g), indicating increased electron density at Yb^{3+} sites.[12] Conversely, Er 4d and Nd 3d/4d peaks in self-sensitized FEM/FNM samples shift positively (Fig. S6), suggesting electron migration toward Yb^{3+} but away from Er^{3+}/Nd^{3+}. This asymmetry arises from differences in electronegativity (Yb > Mo > Er/Nd)[13] and Yb^{3+}'s propensity to stabilize its 4f configuration,[14] supporting MoO_4^{2-}-mediated electron modulation.

Scanning and transmission electron microscopy (SEM/TEM) images (Fig. 1h–j, S7 and S8) reveal similar rod-like morphology (1–3 μm in length) with uniform elemental distribution after thermal activation. High resolution TEM (HRTEM) (Fig. S8) shows ordered lattice arrangement on the edge of rod and small particles with the interplanar spacing of 0.271 and 0.184 nm, corresponding to the (300) and (213) crystal planes of fluorapatite respectively. Dynamic Light Scattering (DLS) analysis (Fig. S9) further confirms polydispersity: primary rods (870.3 nm) with smaller spherical particles (70.7 nm), likely from high-temperature induced crystal growth. Inductively coupled plasma mass spectrometry (ICP-MS) data (Table S5) quantifies dopant incorporation efficacy. Yb : Ln and Mo : P ratios align with initial stoichiometry, while Ca : P ratios (1.47–1.53) deviate slightly from FAp's 1.67, similar to that of hydrothermally synthesized hydroxyapatite and fluorapatite elsewhere.[15]

2.2. Universal UCL enhancement in Yb-sensitized systems

2.2.1. Giant UCL amplification *via* MoO_4^{2-} doping. MoO_4^{2-} doping dramatically enhances UCL across all FYXM samples. For FYEM, the optimal doping (15% Mo) induces a 74-fold enhancement in green emission (510–570 nm) under 980 nm excitation, while red emission (640–680 nm) increases only 2.7-fold (Fig. 2a and d and S10). This green-dominated amplification arises from high excited state energy transfer (HESET) from $|^2F_{7/2}, {}^3T_2\rangle$ towards $^2H_{11/2}/^4S_{3/2}$ and suppressed non-radiative relaxation to lower energy levels. Similar enhancements occur in FYHM and FYTM samples. The UCL of FYHM surges as the doping concentration of MoO_4^{2-} reaches 10%, then drops sharply as increased to 12% (Fig. 2b and e). In the case of FYTM, the optimal concentration is found to be 8% (Fig. 2c and f). Power-dependent log–log slopes (Fig. S11) reveal photon requirements n for population processes. Remarkably, the photon required for the transition of $^1G_4$–$^3H_6$ of Tm^{3+} decreases to a value lower than 2, indicating a two-photon pumping process instead of a three-photon one (Fig. S11c).

Lifetime analysis (Fig. 2g–i, Table S6) reveals prolonged green emission decay for both doped samples: FYEM (129 μs) *versus* FYE (52 μs), and FYHM (137 μs) *versus* FYH (118 μs), reflecting inhibited relaxation towards lower energy levels. Conversely, shortened lifetimes for other emissions suggest additional decay pathways *via* Ln^{3+}/MoO_4^{2-} dimers. Absolute upconversion quantum yield (UCQY) for FYEM reaches 0.004% at 50 W cm^{-2} (Fig. S12, Table 1), comparable to state-of-the-art materials (*e.g.*, $NaYF_4$:Yb^{3+}/Er^{3+}:0.005% at 150 W cm^{-2} (ref. 16)), while uniquely combining high UCL efficiency with inherent biocompatibility.

2.2.2. Mechanism of Ln^{3+}/MoO_4^{2-} dimer-mediated hybridization. Density functional theory (DFT) calculations demonstrate Yb^{3+}/MoO_4^{2-} co-doped fluorapatite unit cell with different substitution patterns in Fig. S13, representing Yb^{3+}-sensitized samples (FYEM, FYHM and FYTM). Considering the much lower concentrations of activator (Er^{3+}/Ho^{3+}/Tm^{3+}) compared with Yb^{3+}, we approximate the unit cell by omitting their presence to avoid constructing a large supercell for further calculation and to focus on interaction between Yb^{3+} and MoO_4^{2-}. The formation energies of crystal cell models with different Yb and Mo substitution sites are calculated and compared in Fig. S14. Notably, the most stable case is case 1 where Yb^{3+} substitutes the Ca1 site adjacent to MoO_4^{2-}. This suggests that Yb^{3+} and MoO_4^{2-} tend to attract each other and favor neighboring substitution inside fluorapatite lattice, which is a prerequisite for interaction of their energy levels.

To obtain a better understanding of the interaction of energy levels of Yb and Mo, we conducted partial density of states (PDOS) analysis of Yb/Mo adjacently substituted case 1, Yb/Mo distantly substituted case 3 with most negative formation energy in each case, and Yb-undoped case as shown in Fig. 3a and b and S15. It is significant that the energy levels of Yb and Mo become overlapped only if Yb occupies the Ca1 site adjacent to Mo. Also, the peak of Yb 4f around Fermi level is broadened as deduced by full width at half maximum (FWHM). These findings confirm the presence of a strong 4d–4f orbital hybridization which causes modification of the electronic structure.[22,23] The redistribution of electrons between Yb and Mo is consistent with the XPS result where electrons flow from Mo towards Yb (Fig. 1e–g).

Fig. 3c–e and S16 illustrate the reflectance of FYXM and other samples. They exhibit characteristic absorption credited to transitions of doped lanthanide ions. Interestingly, the characteristic absorbance of lanthanide ions was generally

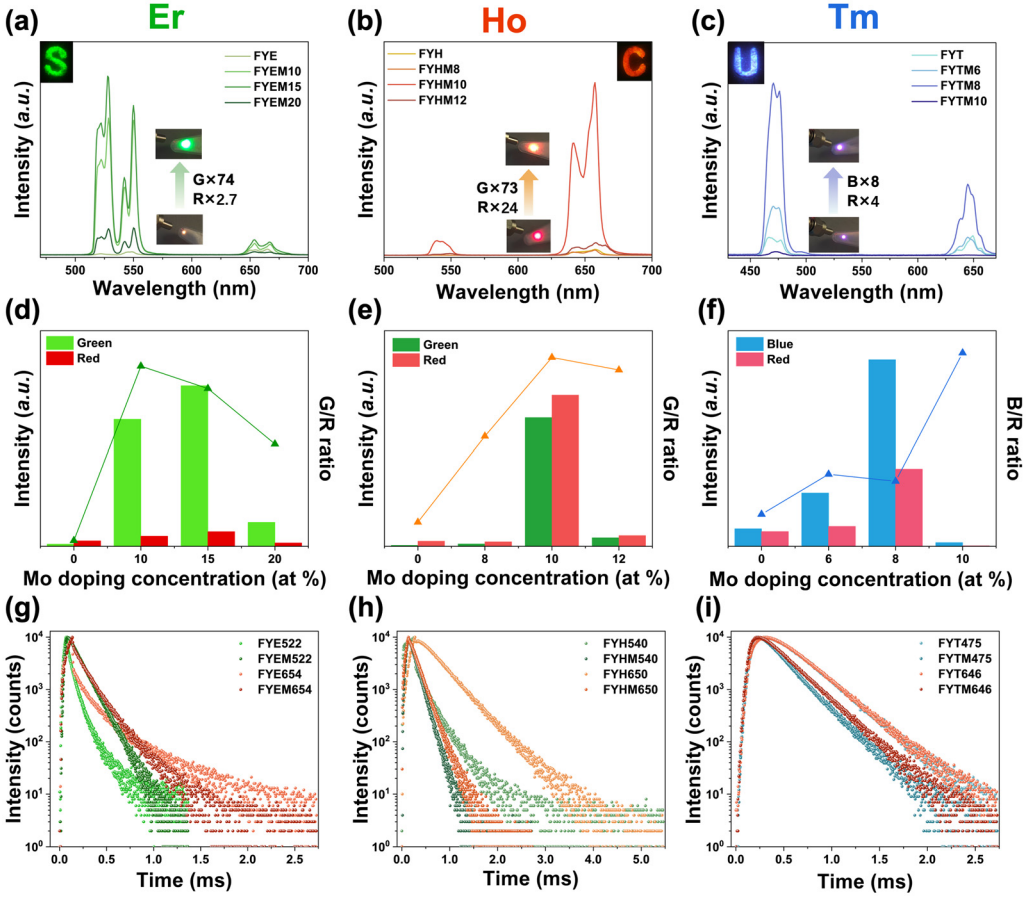

Fig. 2 (a–c) Upconversion luminescence spectra of FYXM samples, with the inset exhibiting luminescent images taken by cellphone with a 700 nm LP optical filter (G, B, R represents integrated luminescence intensity of green, blue, and red emissions respectively). (d–f) Relative intensity of integrated emissions (bar) and corresponding ratios (dotted line) of FYXM samples. (g–i) Upconversion luminescence decay spectra of FYXM samples obtained by time-correlated single photon counting (TCSPC).

Table 1 UCQY comparison of FYEM with benchmark materials

Materials	Power density (W cm^{-2})	UCQY (%)	Ref.
FYEM	**50**	**0.004**	**This work**
SrF_2:Yb^{3+}/Er^{3+}	50	0.002	17
Y_3NbO_7:Yb^{3+}/Er^{3+}	393	0.002	18
$NaLuF_4$:Yb^{3+}/Er^{3+}	33.4	0.004	19
Y_2O_3:Yb^{3+}/Er^{3+}	238	0.004	20
$NaYF_4$:Yb^{3+}/Er^{3+}	150	0.005	16
BZLFT:Yb^{3+}/Er^{3+}	782	0.00016	21

elevated by one time in FYXM samples, which are probably caused by absorption of newly formed energy levels in Yb^{3+}/MoO_4^{2-} dimer. Based on the DFT study and previous analyses, we propose that Ln^{3+} has a tendency to interact with MoO_4^{2-} and having their energy levels recombined.

It is worth mentioning that MoO_4^{2-} owns intrinsic photoluminescence. Specifically, $CaMoO_4$ itself was found to emit green emission peaking at 435 nm under 280 nm excitation, prevailingly attributed to the $^1T_2$–$^1A_1$ allowed transition.[24] We assume that $^1T_1$, $^3T_2$, $^3T_1$ of MoO_4^{2-} could match high energy levels of activator ions and interact with them in energy transfer. Hence, an energy transfer mechanism is proposed and illustrated in Fig. 3f, in which, the energy levels of Yb^{3+} and MoO_4^{2-} are recombined to form new energy levels: $|^2F_{7/2}, {}^1A_1\rangle$ (ground state), $|^2F_{5/2}, {}^1A_1\rangle$, $|^2F_{7/2}, {}^3T_1\rangle$, $|^2F_{7/2}, {}^3T_2\rangle$, $|^2F_{7/2}, {}^1T_1\rangle$ and $|^2F_{7/2}, {}^1T_2\rangle$ (excited state). Specifically, photons are absorbed by ground state absorption (GSA) and excitation state absorption (ESA). Then the energy is transferred from excited state of Yb^{3+}/MoO_4^{2-} dimer towards activator ions, eventually resulting in UCL emissions. The mechanism could also apply to other lanthanide ions, namely Er^{3+} and Nd^{3+} which could also interact in a similar manner.

Interestingly, Yb^{3+}/Er^{3+} co-doped $CaMoO_4$ exhibited UCL with a similarly high G/R ratio as we observed in our experiment.[25] Here we suggest that the Ln^{3+}/MoO_4^{2-} dimer could account for the observed UCL preference. In the case of FYEM, the red emission relies on relaxation from $^2H_{11/2}$/$^4S_{3/2}$ of Er^{3+}, and the larger level gap means less opportunity to get populated, resulting in relatively weak enhancement of red UCL. This preference further confirms the energy transfer mechanism in Fig. 3f, since $^2H_{11/2}$/$^4S_{3/2}$ of Er^{3+} is closer to $|^2F_{7/2}, {}^3T_2\rangle$ than $^4F_{9/2}$. As the concentration further increases beyond

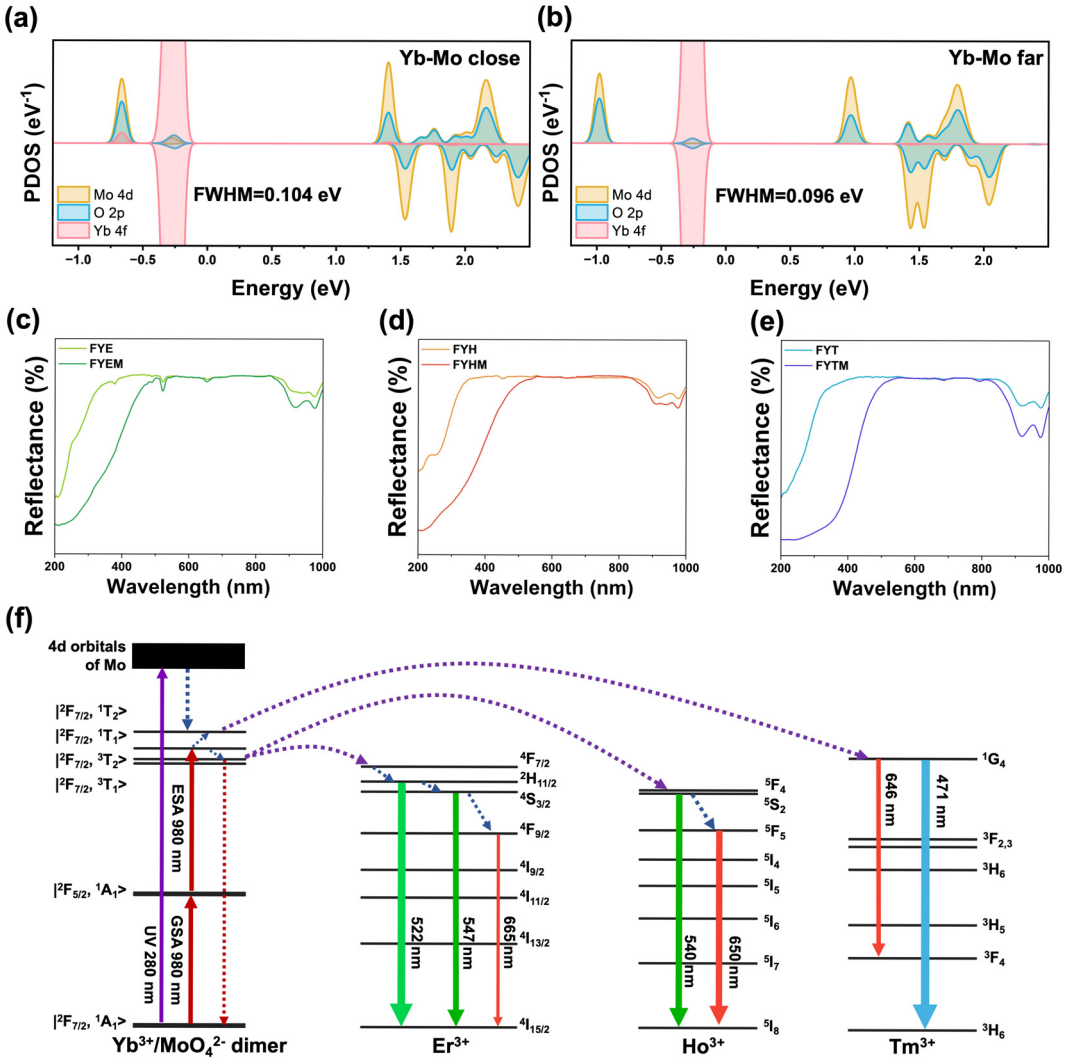

Fig. 3 PDOS of Yb/Mo co-doped fluorapatite where Yb occupies Mo-adjacent Ca1 site (a) and Mo-distant Ca1 site (b) near Fermi level. (c–e) UV-Vis-NIR reflectance spectra of FYX and FYXM samples (X-Er, Ho, or Tm). (f) Proposed energy transfer mechanism diagram in upconversion and downconversion process.

optimal concentration, back energy transfer (BET) process probably prevails over HESET with overall UCL slumping. This could explain why the UCL performance is not in accordance with the content of $CaMoO_4$ phase as more MoO_4^{2-} was doped. In addition, the energy transfer mechanism of Ho/Mo is similar to the Er/Mo combination, both resulting in over 70 times enhancement of UCL. However, a phonon-assisted absorption process is required for the blue emission of Tm^{3+}, which could account for the mere 8-time enhancement of blue emission in Tm/Mo combination.

In order to further examine energy transfer process between MoO_4^{2-} and other lanthanides, the excitation spectra of all samples were performed. As shown in Fig. S17, all FYXM samples exhibit obvious absorption peaks which can be attributed to the transitions of activator ions. Significantly, MoO_4^{2-}-doped samples exhibit a broad absorption band from 250 nm to 320 nm, which corresponds to the O → Mo charge transfer band (CTB). Then we performed emission spectra of FYE and FYXM samples excited at 280 nm (Fig. S18). Since Er^{3+} could not be directly excited by 280 nm excitation, FYE sample did not display any luminescence. On the contrary, the MoO_4^{2-} doped FYEM samples exhibit emission composed of two parts in the region of visible emission: a wide band derived from the intrinsic emission of MoO_4^{2} and sharp green emissions attributed to Er^{3+}. The lifetime at 505 nm is shorter than that at 530 nm or 550 nm, where emission of molybdate overlaps that of Er^{3+} (Fig. S19). The energy transfer process occurs from MoO_4^{2-} towards Er^{3+} and both contribute to the decay, thereby lengthening lifetime at about 20%. And thus, we could draw a conclusion that the excited MoO_4^{2-} group could transfer energy to Er^{3+} ions. Moreover, the green emission of Er^{3+} is prominent than its red emission in the range of 640–675 nm. This indicates the high G/R UCL ratio of FYEM and preference observed in other samples stem

from the energy transfer process mediated by Ln^{3+}/MoO_4^{2-} dimer.

2.3. Breakthrough in self-sensitized systems

Self-sensitized upconversion systems are commonly considered limited by their relatively low efficiency. Herein, we discovered that MoO_4^{2-} can also act as an intrinsic sensitizer in self-sensitized systems (FEM and FNM), eliminating the need for conventional sensitizers (*e.g.*, Yb^{3+}/Nd^{3+}) through direct energy transfer mediated by Ln^{3+}/MoO_4^{2-} dimers—a mechanism analogous to Yb-sensitized systems but with enhanced versatility. Structural properties of FEM/FNM are consistent with FYXM (section 2.1), while their UCL enhancement stems from Ln^{3+}/MoO_4^{2-} dimer-mediated energy transfer (Fig. 4).

Er^{3+} has been found to mediate self-sensitized upconversion (SSU) process under 808 and 980 nm excitation.[26] Doping MoO_4^{2-} brings about UCL enhancement by 23 times and 156 times under 808 nm and 980 nm excitation, respectively (Fig. 4a and b). The mechanism was further assured by luminescence lifetime analysis (Fig. 4c and S20, Tables S7 and S8). The decay time of FEM for emission at 530 nm of Er^{3+} was elongated by 43 times compared with FE suppose that cross relaxation process was less prone to happen in FEM sample, indicative of Er^{3+}/MoO_4^{2-} acting as sensitizer with longer lifetime. Another fact is that under either 808 nm or 980 nm excitation, UCL of FEM shares a similarly high G/R ratio with FYEM and FNYEM. It should be similar to FYEM, where electrons of Er^{3+}/MoO_4^{2-} are more likely to get pumped into $^2H_{11/2}$ and $^4S_{3/2}$ *via* Er^{3+}/MoO_4^{2-} dimer. The power-dependent log–log plot indicates a two-phonon process as given in Fig. S21. Similarly, the energy transfer in FEM is proved by emission spectra under 280 nm excitation in Fig. S22 and S23.

Nd^{3+} is known to own a ladder-like complex 4f energy levels, which favors cross relaxation.[27,28] Although Nd^{3+} is not an excellent SSU candidate, we successfully observed its self-sensitized UCL in Nd^{3+}/MoO_4^{2-} co-doped fluorapatite excited by 808 nm with an 84-fold enhancement in yellow emission ($^2P_{1/2}$–$^4I_{15/2}$) for the first time (Fig. 4d). A preference for yellow UCL was observed as well, as depicted in Fig. S24 by Y/G ratio. Nd^{3+} was found to exhibit photothermal effect under 808 nm excitation through non-radiative relaxation (*e.g.* from $^4F_{5/2}$ to $^4F_{3/2}$) and cross relaxation.[29] Interestingly, after doping MoO_4^{2-}, photothermal effect was enhanced as well (Fig. 4e). The decay spectra were examined and it was found that MoO_4^{2-} doping leads to a shortened lifetime (Fig. 4f). These findings could be credited to Nd^{3+}/MoO_4^{2-} dimer, where more energy levels are created, thus more chances for electrons to be pumped and relaxed. The *n* value is slightly elevated, which is in accordance with that of FYXM and FEM samples (Fig. S25).

2.4. Multi-functional bioapplications enabled by dimer strategy

2.4.1. 808 nm excited upconversion tuning. The dimer strategy not only enhances UCL efficiency but also extends material functionality for multi-wavelength bioapplications. Here, we report the observation of direct 808 nm excitation in MoO_4^{2-}-doped FYEM without Nd^{3+} co-doping (Fig. 5a, S26). Despite low Er^{3+} concentration, the Er^{3+}/MoO_4^{2-} dimer facilitates efficient SSU, achieving a 287-fold UCL amplification compared with FYE. Furthermore, Nd^{3+} was incorporated into FYEM to form FNYEM, enabling stronger dual-wavelength excitation. FNYEM exhibits strong UCL under both 808 nm and 980 nm (further elevating green UCL by 9 folds compared with FYEM under 808 nm excitation), synergistically reducing over-

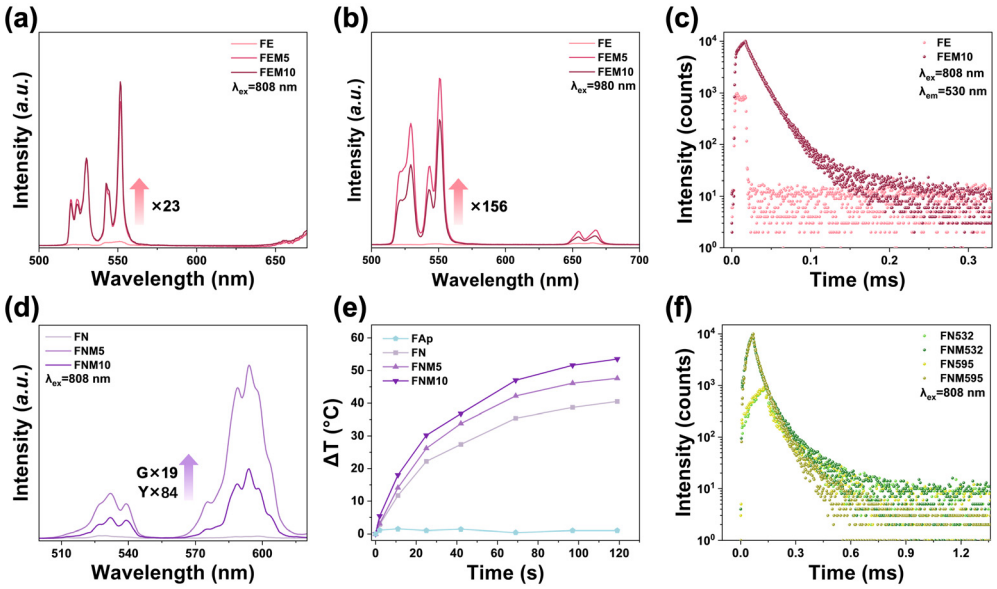

Fig. 4 Upconversion luminescence spectra and decay spectra of FEM (FAp:Er/Mo) samples under 808 nm (a) and 980 nm (b) excitation. (c) Decay spectra of FE and FEM under 808 nm excitation. (d) Upconversion luminescence spectra of FNM (FAp:Nd/Mo) samples under 808 nm excitation. (e) Photothermal heating curves of FAp and FNM under 808 nm excitation. (f) Decay spectra of FN and FNM under 808 nm excitation.

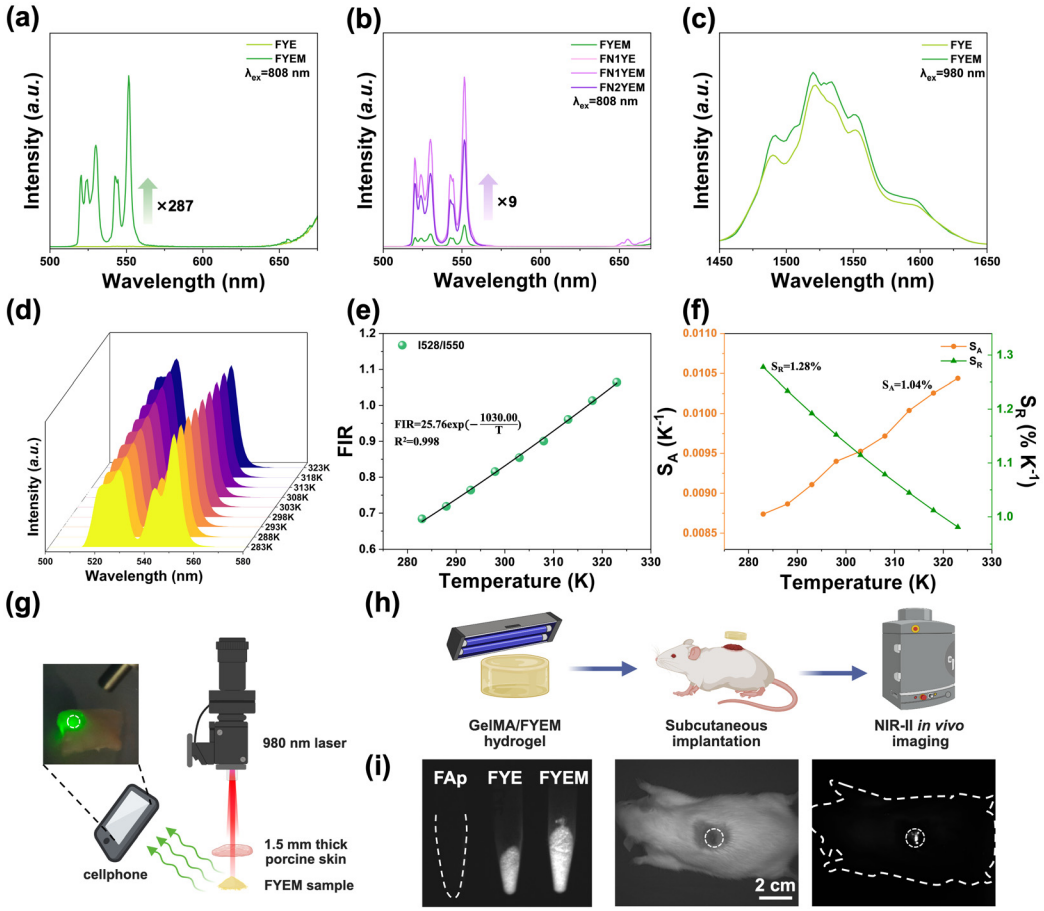

Fig. 5 (a) Upconversion luminescence of FYE and FYEM under 808 nm excitation. (b) Upconversion luminescence of FYEM, FNYE and FNYEM samples under 808 nm excitation. (c) Downconversion luminescence of FYE and FYEM under 980 nm excitation in the region of NIR-II. (d) Temperature-dependent UCL spectra of FYEM under 980 nm excitation. (e) Temperature-FIR curve and fitted data. (f) Temperature-dependent absolute sensitivity (S_A) and relative sensitivity (S_R) curves. (g) *In vitro* imaging process and the inset exhibits the photo taken by a cellphone. (h) Diagram of preparation of GelMA/FYEM hydrogel and *in vivo* imaging process. (i) NIR-II fluorescence images of FAp, FYE and FYEM powders in centrifuge tube under 980 nm excitation (left), bright-field image of mouse implanted with GelMA/FYEM hydrogel subcutaneously (middle) and NIR-II fluorescence images of mouse under 980 nm excitation (right).

heating risks while maintaining high performance, while FNYE exhibits weak UCL under 980 nm and no emission under 808 nm excitation (Fig. 5b, and S27–S29).[30] A significantly prolonged rise time from 62 μs to 117 μs for $^2H_{11/2}$ confirms the additional energy transfer process from Nd^{3+} towards Yb^{3+} when compared with FYEM. Moreover, a high G/R ratio is preserved, consistent with that of FYEM. This dual-excitation capability establishes FNYEM as a versatile platform for deep-tissue theranostics. Although 808 nm excitation minimizes overheating risks,[3] 980 nm excitation provides significantly higher absolute UCL intensity in FYEM due to enhanced energy transfer efficiency *via* Yb^{3+} sensitization. Therefore, for applications requiring maximal signal output (*e.g.*, deep-tissue imaging and thermometry), 980 nm excitation was prioritized in subsequent experiments. Critically, the dimer strategy enables flexible wavelength selection based on specific clinical needs: 808 nm for prolonged *in vivo* safety, and 980 nm for high-sensitivity detection.

2.4.2. NIR-II downconversion luminescence. Leveraging the superior UCL intensity under 980 nm excitation, FYEM's NIR-II DCL was characterized at 980 nm to achieve maximal penetration depth.[31] The Ln^{3+}/MoO_4^{2-} dimer strategy unlocks transformative multifunctionality, extending beyond UCL enhancement to integrated theragnostic platforms. Electrons of Er on $^4I_{11/2}$ could relax to $^4I_{13/2}$ by MPR and thus emit 1530 nm NIR-II emission when backing to ground state. In Fig. 5c we tested the DCL of FYE and FYEM under 980 nm excitation in the region of NIR-II. It could be noted that emission from 1450–1650 nm of FYEM slightly enhances by ~11% compared with FYE, which is credited to the broadened energy levels in Er^{3+}/MoO_4^{2-} dimer. We then examined downconversion quantum yield (DCQY) in the range of 1450–1650 nm under excitation of 980 nm, and the DCQY of FYEM was tested to be 4.87% (Fig. S29). The relatively high DCQY value enables FYEM sample to act as compatible NIR-II bioimaging materials. The DCL of FEM and FNM was studied as well in Fig. S30.

2.4.3. High-sensitivity optical thermometry under physiological temperature. Thermal sensing performance was evaluated under 980 nm excitation to capitalize on FYEM's highest green UCL output, enabling precise fluorescence intensity ratio (FIR) measurements.[32] Based on the thermally coupled energy levels of $^2H_{11/2}$ and $^4S_{3/2}$ and the greatly enhanced green UCL in FYEM and reported results, we measured UCL spectra of FYEM at a temperature range from 283 to 323 K with same excitation power (50 W cm^{-2}, Fig. 5d). According to the Boltzmann distribution law, the FIR values are well fitted to the single-exponential fitting in Fig. 5e, with a correlation coefficient R^2 of 99.8%. As depicted in Fig. 5f, we obtained the maximal value of relative sensitivity (S_R) at 1.28% K^{-1} (283 K), which remains above 1% K^{-1} until 318 K. Moreover, we achieved an extremely high absolute sensitivity (S_A) value, with a minimal value at 0.87% K^{-1} (283 K) and a maximal value at 1.04% K^{-1} (323 K). The S_A value of our FYEM sample is one of the highest values in similar UCL-based optical thermometers, as listed in Table 2. These results indicate that the newly created FYEM material has promising prospects as a candidate for UCL-based optical thermometer utilized for temperature sensing in biomedical applications.

2.4.4. Biocompatible dual-mode imaging. Fig. S31 depicts the cell viability obtained by CCK-8 assay in order to analyze the biocompatibility of FYEM samples by co-culturing with rat osteoblasts. Notably, FYEM sample did not exhibit significant negative effect on rat osteoblasts. Instead, on day 3, FYEM promoted cell proliferation at a concentration of 50 μg mL^{-1} ($^*p < 0.05$). It could be thus concluded that lanthanide/molybdate co-doped FYEM material exhibited favorable cytocompatibility without negative effects on cell growth and proliferation.

Then dual-mode imaging utilized 980 nm excitation for both visible UCL and NIR-II DCL, ensuring consistent high-intensity signals across modalities. The *in vitro* bioimaging of FYEM (Fig. 5g) shows that the porcine skin with a thickness of 1.5 mm is lit up by green UCL of FYEM under 980 nm excitation, suggesting a sufficient UCL intensity for intracutaneous bioimaging. Considering NIR-II DCL is more favorable in deep-tissue bioimaging than visible UCL, the GelMA/FYEM hydrogel is synthesized and placed subcutaneously (section 4.8). The NIR-II DCL of FYEM excited at 980 nm is successfully observed by NIR-II imaging system (Fig. 5i), indicative of remarkable deep-tissue imaging capacity. Conclusively, FYEM proves to be a promising visible/NIR-II dual-mode bioimaging material.

Table 2 Temperature sensing properties of common Yb^{3+}/Er^{3+}-doped UCL optical thermometers

Materials	Excitation wavelength (nm)	S_A@323 K (% K^{-1})	Ref.
FYEM	**980**	**1.04**	**This work**
$NaYF_4$:$Yb^{3+}/Er^{3+}/Nd^{3+}$	980	0.23	33
K_3ZrF_7:Yb^{3+}/Er^{3+}	980	0.23	34
$NaGdF_4$:$Yb^{3+}/Er^{3+}/Fe^{3+}$	980	0.27	35
$La_{9.67}Si_6O_{26.5}$:$Yb^{3+}/Er^{3+}/Ho^{3+}$	980	0.31	36
$Gd_2Te_6O_{15}$:Yb^{3+}/Er^{3+}	980	0.35	37
$NaYTiO_4$:$Yb^{3+}/Er^{3+}/Sc^{3+}$	980	0.36	38
Y_2O_3:Yb^{3+}/Er^{3+}	980	0.47	39
Li_2HfO_3:Yb^{3+}/Er^{3+}	980	0.58	40
YVO_4:Yb^{3+}/Er^{3+}	980	0.58	41
$NaY(WO_4)_2$:Yb^{3+}/Er^{3+}	980	0.66	42
Ca_2MgWO_6:Yb^{3+}/Er^{3+}	980	0.76	43
HAp/β-TCP:Yb/Er/Mo/Sr	980	0.88	44

3. Conclusions

In this work, we have developed a universal MoO_4^{2-}-doping strategy to boost UCL in lanthanide-doped fluorapatite *via* 4d–4f orbital hybridization. The formation of stable Ln^{3+}/MoO_4^{2-} dimer significantly enhances energy transfer efficiency, achieving remarkable UCL amplifications (UCQY = 0.004%). Crucially, this mechanism is demonstrated for the first time in self-sensitized systems (Er^{3+}/Nd^{3+}), overcoming traditional reliance on Yb^{3+} as sensitizer. The optimized material integrates multifunctionality—including dual-wavelength excitation (808/980 nm), NIR-II deep-tissue imaging (DCQY = 4.87%), and record-high temperature sensitivity (S_A = 1.04% K^{-1}@323 K). This work establishes a versatile platform for next-generation deep-tissue diagnostics, photothermal therapy, and real-time physiological monitoring.

4. Methods

4.1. Materials

$Ca(NO_3)_2{\cdot}4H_2O$, NaOH and ethanol were obtained from Kelong Chemical Reagents Company, China. $Yb(NO_3)_3{\cdot}5H_2O$, $Tm(NO_3)_3{\cdot}6H_2O$, $Ho(NO_3)_3{\cdot}5H_2O$, $Er(NO_3)_3{\cdot}6H_2O$, $Nd(NO_3)_3{\cdot}5H_2O$ and $(NH_4)_6Mo_7O_{24}{\cdot}4H_2O$ were obtained from Macklin Co. Ltd, Shanghai, China. NaF and $(NH_4)_2HPO_4$ were obtained from Aladdin Co. Ltd, Shanghai, China. All the chemical reagents were of analytical grade and used without further purification.

4.2. Synthesis of FYX samples

The FAp:Yb/X (X = Er, Ho, or Tm) co-doped upconversion fluorapatites (FYX) were hydrothermally synthesized based on a previous method with some modification. Taking FYE as an example, an aqueous solution of $(NH_4)_2HPO_4$ and NaF was added drop by drop into the mixture solution of $Ca(NO_3)_2$, $Yb(NO_3)_3$, $Er(NO_3)_3$ under vigorous stirring. The molar concentrations of Yb^{3+} and Er^{3+} ions relative to Ca^{2+} ions were set at 10 : 0.5 : 89.5 (Table S1), and the ratio of [(Ca + Ln)/P] was kept constant at 1.67. The 1 M NaOH stock solution was added drop by drop to maintain the pH at 9–10. The solution was further stirred for 30 min to obtain a white slurry. The slurry was then transferred into a 100 mL Teflon-lined autoclave and hydrothermally treated at 180 °C for 6 h. The obtained precipitates were centrifuged (5 min at 2700*g*) and fully washed with deionized water and ethanol for three times. Finally, samples were fully lyophilized, ground into white powder and sintered

at 900 °C for 2 h to activate the upconversion luminescence. Other Mo-free FYX samples were synthesized in a similar pattern.

4.3. Synthesis of Mo-doped FYXM samples

Yb/X/Mo (X = Er, Ho, or Tm) tri-doped fluorapatites were synthesized with MoO_4^{2-} partially substituting PO_4^{3-}, lanthanide partially substituting Ca^{2+} in a similar approach according to our previous research. The molar ratio of Yb^{3+} and Tm^{3+}/Ho^{3+}/Er^{3+} was set to be 20 : 0.1, 10 : 0.1, and 10 : 0.5, respectively,[45] keeping a constant [(Ca + Ln)/(P + Mo)] molar ratio of 1.67 (Table S1). Samples were then collected and sintered as mentioned above. For the sake of brevity, FYTM8, FYHM10 and FYEM15 samples with optimal UCL properties were designated FYTM, FYHM and FYEM in the following sections if not specified.

The self-sensitized Er^{3+}/MoO_4^{2-}, Nd^{3+}/MoO_4^{2-}, or Nd^{3+}/Yb^{3+}/Er^{3+}/MoO_4^{2-} co-doped fluorapatite materials were synthesized by similar means and were designated FNYEM, FEM, FNM respectively (Table S2).

4.4. Characterization

The phase composition of all samples was tested by X-ray diffraction (XRD) PANalytical Empyrean equipment (U.K.) in the 2θ range from 20° to 70° with Cu Kα radiation (λ = 1.5406 Å). TG-DSC curves were obtained in air by using Netzsch STA449 F3 Jupiter (Germany). The morphology of particles was observed by scanning electron microscopy (SEM) of Thermo Fisher Scientific Apreo 2C (U.S.) and transmission electron microscopy (TEM) using JEM-F200, JEOL (Japan). The ratio of ions was tested by inductively coupled plasma-mass spectrometry (ICP-MS) of Agilent 7800 (U.S.). The Fourier transform infrared (FTIR) spectra were conducted from Thermo Fisher Nicolet (U.S.) with a wavenumber range of 400–3000 cm^{-1}. UV-Vis-NIR diffuse reflectance spectra (UV-Vis-NIR DRS) were conducted using Shimadzu UV 3600 (Japan). The dynamic light scattering (DLS) was tested using Litesizer 500, Anton Paar (Australia), by dispersing samples in ethanol. The X-ray photoelectron spectroscopy (XPS) was recorded by Thermo Fisher Scientific K-Alpha (U.S.). The photoluminescence (PL) excitation/emission spectra were performed by using Horiba JobinYvon Fluorologs-3 spectrofluorometer (Japan) with an external 808/980 diode laser (MDL-III-808/MDL-H-980) for upconversion, or Xenon lamp for downconversion as the excitation source with appropriate optical filter. All UCPL spectra were obtained with an excitation power ranging from 0.3–1.5 W based on relative intensity of samples and an integration time no more than 0.5 s, with a 700 nm short-pass optical filter. Diode lasers and optical filters were obtained from Changchun New Industries Optoelectronics Technology Co., Ltd, China. Fluorescence lifetime was measured with appropriate excitation source and a picosecond photon detection module (PPD-850) as the detector. Upconversion quantum yield (UCQY) was studied using ATP65, OPTOSKY (China), excited by 980 nm diode laser at ~50 W cm^{-2}. Downconversion quantum yield (DCQY) was tested by Fluorolog-QM, Horiba (Japan). All tests were conducted under room temperature without further clarification. The photothermal performance was recorded with a PTi120 thermal camera, Fluke (U.S.).

4.5. Upconversion luminescence lifetime study

The time dependence of the UCL intensity in the decay phase could be described as

$$I(t) = I_0 + A_1 \exp\left(-\frac{t}{\tau_{d1}}\right) + +A_2 \exp\left(-\frac{t}{\tau_{d2}}\right) + \dots \quad (1)$$

where A is a fitting parameter and I_0 is the offset parameter. τ_{di} is an exponential component of decay time, and the average decay time is expressed as

$$\tau_{decay} = \frac{\sum A_i {\tau_{di}}^2}{\sum A_i \tau_{di}} \quad (2)$$

In order to assess the rise phase, the rise time τ_{rise} is defined as the time needed to reach up to $(1 - e^{-1})I_{max}$, where I_{max} is set 1000, 2000 or 10 000 according to the UCL intensity of each sample.[46]

4.6. Temperature-dependent upconversion luminescence study

According to the Boltzmann distribution law, the FIR can be expressed as

$$FIR = \frac{I_{522}}{I_{550}} = B \exp\left(-\frac{\Delta E}{k_B T}\right) \quad (3)$$

where I_{522} and I_{550} are the peak emission intensities for $^2H_{11/2}$ and $^4S_{3/2}$, and ΔE is the energy gap between them. B, k_B and T correspond to constant, Boltzmann constant, and the absolute temperature, respectively. Sensitivity is a key parameter to assess the performance of an optical thermometer. The absolute sensitivity (S_A) and relative sensitivity (S_R) are calculated according to the following equations:[32]

$$S_A = \frac{dFIR}{dT} = FIR\frac{\Delta E}{k_B T^2} \quad (4)$$

$$S_R = \frac{1}{FIR}\frac{dFIR}{dT} \times 100\% = \frac{\Delta E}{k_B T^2} \times 100\% \quad (5)$$

4.7. Cytocompatibility assay

To evaluate the cytocompatibility of lanthanide/molybdate co-doped samples, rat osteoblasts were cocultured with FYEM nanoparticles in various concentrations (0, 50, 100, and 200 μg mL^{-1}). The cells were cultured in minimum essential medium–alpha modification (α-MEM, GIBCO, USA) supplemented with 10% newborn bovine calf serum (NBCS, GIBCO, USA) and 1% penicillin–streptomycin solution (100 U mL^{-1}, GIBCO). The cells were incubated at 37 °C under conditions of 5% carbon dioxide and 90% humidity. Cell proliferation was then assessed by using a CCK-8 kit (APExBIO, USA), on days 1, 3, and 7.

4.8. *In vitro* and *in vivo* imaging

In vitro imaging in the region of visible light was conducted by placing FYEM sample under a piece of porcine skin with a thickness of 1.5 mm. A cellphone (Xiaomi 11 Pro, China) was used with an 850 nm short-pass optical filter to record the emitted green upconversion luminescence of FYEM under 980 nm excitation. The NIR-II DC luminescence was imaged using a Series III 800 NIR-II imaging system (Suzhou NIR-Optics Technologies Co., Ltd, China), with a 1300 nm long-pass optical filter. FAp, FYE, and FYEM samples were placed in centrifuge tubes and their NIR-II luminescence was observed under 980 nm excitation with pumping power at 1 W and acquisition time at 20 ms.

In order to immobilize FYEM powder during *in vivo* imaging experiment, the sample is mixed with GelMA hydrogel. The synthesis of GelMA hydrogel is given elsewhere.[47] The GelMA/FYEM hydrogel was cured under UV lamp in a circular mold and then implanted subcutaneously in an 8-week Sprague-Dawley (SD) rat to demonstrate the ability of NIR-II bioimaging capacity in subcutaneous tissue with an average tissue thickness at about 3 mm. All animal experiments were approved by the Research Ethics Committee of West China Hospital of Stomatology (No. WCHSIRB-D-2024-744). All procedures were carried out following the ARRIVE guidelines and related principles of the care and use of laboratory animals. The NIR-II fluorescence was collected by the same NIR-II imaging system with pumping power at 3 W and acquisition time at 200 ms.

4.9. Theoretical calculation

All of the calculations are performed in the framework of the spin-polarized density functional theory with the projector augmented plane-wave method, as implemented in the Vienna *ab initio* simulation package (VASP).[48,49] The generalized gradient approximation (GGA) proposed by Perdew, Burke, and Ernzerhof (PBE) is selected for the exchange–correlation potential.[50,51] The long-range van der Waals interaction is described by the DFT-D3 approach.[52] DFT+*U* method with the effective *U* value of 3.5 eV and 6 eV has been used to correct the influence of 4d electrons of Mo and Yb atoms. The cut-off energy for plane wave is set to 480 eV. The energy criterion is set to 10^{-5} eV in iterative solution of the Kohn–Sham equation. All the structures are relaxed until the residual forces on the atoms have declined to less than 0.02 eV $Å^{-1}$. Data analysis and visualization are carried out with the help of VASPKIT[53] code and VESTA.[54] To avoid interlaminar interactions, a vacuum spacing of 20 Å is applied perpendicular to the slab.

The formation energy E_{form} is expressed as

$$E_{form} = E_{defect} - E_{perfect} - E_{Yb} + E_{Ca} \quad (6)$$

where E_{defect} and $E_{perfect}$ are the energy with and without the defect. E_{Ca} and E_{Yb} are the chemical potentials of Ca and Yb, respectively.

4.10. Statistical analysis

Quantitative data were presented as mean ± standard deviation (SD) value. Data from different groups were statistically compared *via* one-way analysis of variance (ANOVA). The level of significance was set as $*p < 0.05$, $**p < 0.01$, $***p < 0.001$, $****p < 0.0001$.

Author contributions

X. L. conceived and directed the research; B. W. prepared the fluorapatite nanocrystals with assistance from Y. R., W. Y., Y. L. and J. L.; B. W. collected and analyzed most of the experimental data, with contributions from X. W. and J. L.; B. W. and H. S. discussed and interpreted the DFT calculation data; all authors contributed to the data analysis; the manuscript was written by B. W. and X. L.

Conflicts of interest

The authors declare that there are no competing financial interests or personal relationships that could have appeared to influence the work reported in this paper.

Data availability

The data supporting this article have been included as part of the supplementary information (SI), including supporting notes, additional experimental and calculated results, and summaries of dopant molar concentration in synthesis and luminescence rise and decay lifetimes. Supplementary information is available. See DOI: **https://doi.org/10.1039/d5qi01918d**.

Acknowledgements

This work was supported by the National Key Research and Development Program of China (Grants No. 2021YFA1201302), the Fund from Science and Technology Department of Sichuan Province, China (Grant No. 2023NSFSC1930), and Tianfu Qingcheng Plan-Youth Science and Technology Talent Project, Sichuan, China (Grant No. 1710). We would like to express our genuine gratitude to Dr Peng Wu and Dr Yanying Wang of Analytical & Testing Center, Sichuan University, for their assistance with fluorescence testing and analysis. We acknowledge the use of BioRender for creating Fig. 1a, 5g and h (**https://BioRender.com/ob4f13u**).

References

1 S. Lamon, H. Yu, Q. Zhang and M. Gu, Lanthanide ion-doped upconversion nanoparticles for low-energy super-resolution applications, *Light: Sci. Appl.*, 2024, **13**(1), 252.

2 R. S. Ajee, P. S. Roy, S. Dey and S. Sundaresan, Upconversion nanoparticles and their potential in the realm of biomedical sciences and theranostics, *J. Nanopart. Res.*, 2024, **26**(3), 50.
3 Z. Yi, Z. Luo, X. Qin, Q. Chen and X. Liu, Lanthanide-activated nanoparticles: a toolbox for bioimaging, therapeutics, and neuromodulation, *Acc. Chem. Res.*, 2020, **53**(11), 2692–2704.
4 X. Li, Q. Zou, L. Chen and W. Li, A ternary doped single matrix material with dual functions of bone repair and multimodal tracking for applications in orthopedics and dentistry, *J. Mater. Chem. B*, 2018, **6**(38), 6047–6056.
5 X. Li and H. Chen, Yb^{3+}/Ho^{3+} co-doped apatite upconversion nanoparticles to distinguish implanted material from bone tissue, *ACS Appl. Mater. Interfaces*, 2016, **8**(41), 27458–27464.
6 B. Nasiri-Tabrizi, W. J. Basirun, C. H. Yeong and W. M. Thein, Development of the third generation of bioceramics: Doping hydroxyapatite with s-, p-, d-, and f-blocks cations and their potential applications in bone regeneration and void filling, *Ceram. Int.*, 2023, **49**(5), 7142–7179.
7 S. Mohanty and A. M. Kaczmarek, Unravelling the benefits of transition-metal-co-doping in lanthanide upconversion nanoparticles, *Chem. Soc. Rev.*, 2022, **51**(16), 6893–6908.
8 M. Matakgane, T. Mokoena and M. Mhlongo, Recent trends of oxides heterostructures based upconversion phosphors for improving power efficiencies of solar cells: A review, *Inorg. Chem. Commun.*, 2023, **156**, 111202.
9 X. Li, Q. Zou, Y. Man and W. Li, Synergistic effects of novel superparamagnetic/upconversion HA material and Ti/magnet implant on biological performance and long–term in vivo tracking, *Small*, 2019, **15**(31), 1901617.
10 H. N. Van, N. H. Vu, V.-H. Pham, *et al.*, A novel upconversion emission material based on Er^{3+}-Yb^{3+}-Mo^{6+} tridoped Hydroxyapatite/Tricalcium phosphate (HA/β-TCP), *J. Alloys Compd.*, 2020, **827**, 154288.
11 M. A. Goldberg, N. O. Donskaya, D. V. Valeev, *et al.*, Mesoporous molybdate-substituted hydroxyapatite nanopowders obtained via a hydrothermal route, *Ceram. Int.*, 2024, **50**(10), 17404–17418.
12 F. Li, P. Wang, T. Zhang, *et al.*, Efficient Removal of Antibiotic Resistance Genes through 4f–2p–3d Gradient Orbital Coupling Mediated Fenton–Like Redox Processes, *Angew. Chem., Int. Ed.*, 2023, **62**(47), e202313298.
13 M. Rahm, T. Zeng and R. Hoffmann, Electronegativity seen as the ground-state average valence electron binding energy, *J. Am. Chem. Soc.*, 2019, **141**(1), 342–351.
14 G. H. Debnath, P. Mukherjee and D. H. Waldeck, Identifying Lanthanide Energy Levels in Semiconductor Nanoparticles Enables Tailored Multicolor Emission through Rational Dopant Combinations, *Acc. Chem. Res.*, 2025, **58**(9), 1473–1483.
15 A. Wang, H. Yin, D. Liu, *et al.*, Size-controlled synthesis of hydroxyapatite nanorods in the presence of organic modifiers, *Mater. Lett.*, 2007, **61**(10), 2084–2088.
16 J.-C. Boyer and F. C. Van Veggel, Absolute quantum yield measurements of colloidal $NaYF_4$: Er^{3+}, Yb^{3+} upconverting nanoparticles, *Nanoscale*, 2010, **2**(8), 1417–1419.
17 S. Balabhadra, M. L. Debasu, C. D. Brites, R. A. Ferreira and L. D. Carlos, Upconverting nanoparticles working as primary thermometers in different media, *J. Phys. Chem. C*, 2017, **121**(25), 13962–13968.
18 F. H. Borges, J. C. Martins, F. J. Carlos, R. A. Ferreira and R. R. Gonçalves, Luminescent thermometry based on Er^{3+}/Yb^{3+} co-doped yttrium niobate with high NIR emission and NIR-to-visible upconversion quantum yields, *J. Lumin.*, 2022, **248**, 118986.
19 F. You, S. Zheng, T. Pang, *et al.*, Transparent Ho^{3+}/Tm^{3+}/Er^{3+}/Yb^{3+} Codoped Nano–Glass–Ceramics for Upconversion Head–Up Display, *Laser Photonics Rev.*, 2024, **18**(12), 2400838.
20 M. L. Debasu, J. C. Riedl, J. Rocha, L. D. Carlos, *et al.*, The role of Li^+ in the upconversion emission enhancement of $(YYbEr)_2O_3$ nanoparticles, *Nanoscale*, 2018, **10**(33), 15799–15808.
21 J. Yang, P. Lin, E. Y. B. Pun, J. Yuan, X. Zhao, H. Lin, *et al.*, Quantification of upconversion photon and thermosensitive feedback in Er^{3+}/Yb^{3+} doped fluorotellurite glasses, *J. Lumin.*, 2020, **222**, 117184.
22 J. Wen, S. Hui, Q. Chang, *et al.*, Enhancement of Electromagnetic Wave Attenuation through Polarization Loss Induced by Hybridization of Rare–Earth 4f and Mo–4d Orbitals in Liquid Plasma, *Adv. Funct. Mater.*, 2024, **34**(51), 2410447.
23 X. Wang, L. Shi, W. Ren, *et al.*, Enhancing* CO coverage on Sm-Cu_2O via 4f-3d orbital hybridization for highly efficient electrochemical CO_2 reduction to C_2H_4, *J. Energy Chem.*, 2024, **99**, 409–416.
24 A. Phuruangrat, T. Thongtem and S. Thongtem, Preparation, characterization and photoluminescence of nanocrystalline calcium molybdate, *J. Alloys Compd.*, 2009, **481**(1–2), 568–572.
25 S. Gouraha, S. Sinha, A. Srivastava and J. Singh, Microwave assisted preparation of ternary scheelite $CaMoO_4$: Er^{3+}/Yb^{3+} nano-phosphors for up/down-conversion photoluminescence, temperature sensing and antibacterial properties, *J. Photochem. Photobiol., A*, 2025, **458**, 115967.
26 L. Yan, B. Zhou, N. Song, *et al.*, Self-sensitization induced upconversion of Er^{3+} in core–shell nanoparticles, *Nanoscale*, 2018, **10**, 17949–17957.
27 Z. Yu, W. K. Chan and T. T. Y. Tan, Neodymium–sensitized nanoconstructs for near–infrared enabled photomedicine, *Small*, 2020, **16**(1), 1905265.
28 Z. Yu, W. Hu, H. Zhao, *et al.*, Generating New Cross–Relaxation Pathways by Coating Prussian Blue on $NaNdF_4$ To Fabricate Enhanced Photothermal Agents, *Angew. Chem., Int. Ed.*, 2019, **58**(25), 8536–8540.
29 L. Ma, Y. Zhou, Z. Zhang, *et al.*, Multifunctional bioactive Nd-Ca-Si glasses for fluorescence thermometry, photothermal therapy, and burn tissue repair, *Sci. Adv.*, 2020, **6**(32), eabb1311.

30 S. Liu, Z. An and B. Zhou, Optical multiplexing of upconversion in nanoparticles towards emerging applications, *Chem. Eng. J.*, 2023, **452**, 139649.
31 P. Du, R. An, Y. Liang, P. Lei and H. Zhang, Emerging NIR-II luminescent bioprobes based on lanthanide-doped nanoparticles: from design towards diverse bioapplications, *Coord. Chem. Rev.*, 2022, **471**, 214745.
32 H. Liang, K. Yang, Y. Yang, *et al.*, A lanthanide upconversion nanothermometer for precise temperature mapping on immune cell membrane, *Nano Lett.*, 2022, **22**(22), 9045–9053.
33 B. Cao, Y. Bao, Y. Liu, *et al.*, Wide-range and highly-sensitive optical thermometers based on the temperature-dependent energy transfer from Er to Nd in Er/Yb/Nd codoped NaYF4 upconversion nanocrystals, *Chem. Eng. J.*, 2020, **385**, 123906.
34 H. Fu, W. Xie, Y. Qian, *et al.*, Ultrafast Room–Temperature Synthesis of Yb^{3+}/Er^{3+} Codoped K_3ZrF_7 Nanocrystals for Thermal Enhancement of Upconversion, *Laser Photonics Rev.*, 2025, **19**(5), 2401522.
35 J. Tang, P. Du, W. Li and L. Luo, Boosted thermometric performance in $NaGdF_4$: Er^{3+}/Yb^{3+} upconverting nanorods by Fe^{3+} ions doping for contactless nanothermometer based on thermally and non-thermally coupled levels, *J. Lumin.*, 2020, **224**, 117296.
36 J. Zhang, J. Chen and Y. Zhang, Temperature-sensing luminescent materials $La_{9.67}Si_6O_{26.5}$: Yb^{3+}–Er^{3+}/Ho^{3+} based on pump-power-dependent upconversion luminescence, *Inorg. Chem. Front.*, 2020, **7**(24), 4892–4901.
37 H. Liang, X. Lin, N. Ma, *et al.*, Up–conversion luminescence of Er^{3+}/Yb^{3+} co–doped $Gd_2Te_6O_{15}$ tellurite glass–ceramics for optical thermometry, *J. Am. Ceram. Soc.*, 2024, **107**(12), 8191–8205.
38 Y. Wang, C. Zuo, C. Ma, *et al.*, Effects of Sc^{3+} ions on local crystal structure and up-conversion luminescence of layered perovskite $NaYTiO_4$: Yb^{3+}/Er^{3+}, *J. Alloys Compd.*, 2021, **876**, 160166.
39 R. Ao, L. Xing and W. Yang, A high-brightness phosphor based on Yb^{3+}/Er^{3+} codoped Y_2O_3 micro-crystals and controllable temperature sensing sensitivity via rare earth ions, *Opt. Commun.*, 2021, **492**, 126967.
40 R. An, Y. Liang, R. Deng, P. Lei and H. Zhang, Hollow nanoparticles synthesized via Ostwald ripening and their upconversion luminescence-mediated Boltzmann thermometry over a wide temperature range, *Light: Sci. Appl.*, 2022, **11**(1), 217.
41 M. Jia, Z. Sun, M. Zhang, H. Xu and Z. Fu, What determines the performance of lanthanide-based ratiometric nanothermometers?, *Nanoscale*, 2020, **12**(40), 20776–20785.
42 M. Lin, L. Xie, Z. Wang, B. S. Richards, G. Gao and J. Zhong, Facile synthesis of mono-disperse sub-20 nm $NaY(WO_4)_2$: Er^{3+}, Yb^{3+} upconversion nanoparticles: a new choice for nanothermometry, *J. Mater. Chem. C*, 2019, **7**(10), 2971–2977.
43 Y. Jiang, Y. Tong, S. Chen, *et al.*, A three-mode self-referenced optical thermometry based on up-conversion luminescence of Ca_2MgWO_6: Er^{3+}, Yb^{3+} phosphors, *Chem. Eng. J.*, 2021, **413**, 127470.
44 H. N. Van, D.-H. Nguyen and V.-H. Pham, Effect of Sr substituted on multifunction pure green emission of rare-earth-element doped HA/β-TCP nanocomposite for optical thermometer, *Ceram. Int.*, 2024, **51**(12), 16894–16903.
45 J. Tang, P. Du, W. Li and L. Luo, Boosted thermometric performance in $NaGdF_4$: Er^{3+}/Yb^{3+} upconverting nanorods by Fe^{3+} ions doping for contactless nanothermometer based on thermally and non-thermally coupled levels, *J. Lumin.*, 2020, **224**, 117296.
46 S. J. W. Vonk, J. J. E. Maris, A. J. H. Dekker, *et al.*, Rise and Decay of Photoluminescence in Upconverting Lanthanide-Doped Nanocrystals, *ACS Nano*, 2024, **18**(41), 28325–28334.
47 Q. Wei, J. Su, S. Meng, *et al.*, MiR-17-5p-engineered sEVs Encapsulated in GelMA Hydrogel Facilitated Diabetic Wound Healing by Targeting PTEN and p21, *Adv. Sci.*, 2024, **11**, 2307761.
48 G. Kresse and J. Hafner, *Ab initio* molecular dynamics for open-shell transition metals, *Phys. Rev. B: Condens. Matter Mater. Phys.*, 1993, **48**(17), 13115–13118.
49 G. F. L. Kresse and J. Furthmüller, Efficient iterative schemes for *ab initio* total-energy calculations using a plane-wave basis set, *Phys. Rev. B: Condens. Matter Mater. Phys.*, 1996, **54**(11), 169–185.
50 J. P. Perdew, K. Burke and M. Ernzerhof, Generalized gradient approximation made simple, *Phys. Rev. Lett.*, 1996, **77**(18), 3865–3868.
51 W. Kohn and L. J. Sham, Self-Consistent Equations Including Exchange and Correlation Effects, *Phys. Rev.*, 1965, **140**(4A), A1133–A1138.
52 S. Grimme, J. Antony, S. Ehrlich and H. Krieg, A consistent and accurate ab initio parametrization of density functional dispersion correction (DFT-D) for the 94 elements H-Pu, *J. Chem. Phys.*, 2010, **132**(15), 154104.
53 V. Wang, N. Xu, J.-C. Liu, G. Tang and W.-T. Geng, VASPKIT: A user-friendly interface facilitating high-throughput computing and analysis using VASP code, *Comput. Phys. Commun.*, 2021, **267**, 108033.
54 K. Momma and F. Izumi, VESTA: a three-dimensional visualization system for electronic and structural analysis, *J. Appl. Crystallogr.*, 2008, **41**(3), 653–658.